







Deterministic preparation of a dual-species two-ion crystal

Maximilian J. Zawierucha ^{1,2,*}, Till Rehmert ^{1,2,*}, Jonas Keller ¹, Tanja E. Mehlstäubler ^{1,2},
Piet O. Schmidt ^{1,2} and Fabian Wolf ^{1,‡}

¹*Physikalisch-Technische Bundesanstalt, Bundesallee 100, 38116 Braunschweig, Germany*

²*Institut für Quantenoptik, Leibniz Universität Hannover, Welfengarten 1, 30167 Hannover, Germany*



(Received 6 March 2024; accepted 7 June 2024; published 8 July 2024)

The demand for efficient preparation methods for dual-species ion crystals is rapidly expanding across quantum technology and fundamental physics applications with trapped ions. We present a deterministic and efficient technique to produce such crystals, utilizing the segmented structure of a linear Paul trap. By precisely tailoring the trapping potentials, we can split, move, and discard parts of an ion chain. This process is automated in a sequence that converts a larger ion sample into the desired configuration. A critical component of our approach is the accurate identification of crystal constituents. This is achieved by matching the measured positions of fluorescing ions against theoretical expectations for larger crystals, thus facilitating the detection of nonfluorescing ions and enabling accurate ion counting. We demonstrate that our method reliably produces two-ion crystals within minutes. These results represent a significant advance in the production of two-species ion crystals with applications ranging from quantum logic spectroscopy and optical clocks to quantum computing and simulations with trapped ions.

DOI: [10.1103/PhysRevA.110.013107](https://doi.org/10.1103/PhysRevA.110.013107)

I. INTRODUCTION

Trapped ions have been established as a versatile platform for advancing the field of atomic, molecular, and optical physics over the past few decades. Unprecedented accuracies in trapped-ion clocks [1–5], highly sensitive sensors [6–12], and quantum computers [13–15] are just some of the outstanding applications which are being pursued. While many of these experiments are possible with a single species of ions, extending the control capabilities to dual-species ion systems enables a richer variety of experiments and is even a necessity for certain applications. For instance, cotrapped ions of different species can serve as an *in situ* sensor for perturbing fields [16–18] or for sympathetic cooling of an ion species with no (accessible) laser-cooling transition [19–34]. The latter has enabled the development of optical quantum logic clocks [2,35–38] and precision spectroscopy on highly charged [39,40] and molecular [41,42] ions and helps to preserve coherence for quantum information processing [43,44].

Here, we present a technique for preparing such a dual-species two-ion crystal. The process relies on modifying the confining dc potentials to iteratively split a dual-species ion chain. The constituents of each subcrystal are detected, and

the more favorable one is kept in the trap, while the other one is expelled from the trap. Repeating this process successively reduces the size of the ion chain, finally leading to a dual-species two-ion crystal. While the composition of the subsamples after the splitting operation is probabilistic, the possibility of remerging and repeating the splitting renders the entire preparation scheme deterministic. Ion detection is based on position-resolved fluorescence detection of one ion species and, from that, inferring the other nonfluorescing ion species' position.

Different techniques can be used to load ions into a radio-frequency trap, such as ionizing an atomic vapor from an electrically [45] or optically [46] heated oven, using a laser-cooled atomic cloud [47,48], or ablating atoms with a laser [49,50]. All of those approaches have advantages and drawbacks.

Typically, oven loading is slower than ablation loading. More rapid buildup of atom flux for faster loading can be achieved by increasing the oven temperature [45] but leads to a high background pressure inside the vacuum chamber. Loading from a precooled ensemble of atoms requires substantial technical overhead and suitable laser-cooling transitions for the atomic species. For ablation loading, there is a trade-off between fast loading and control over the exact number of ions since the loading process is governed by Poisson statistics [49], which means that higher laser intensities yield a higher probability of successful loading but result in a loss of control over the ion number. Additionally, variations in beam pointing, target surface degradation, and laser intensity have a strong impact on the number of loaded ions [50–56].

These limitations for ablation loading can be alleviated by subtractive preparation schemes, where a larger ion crystal is loaded and then reduced to the desired size by remov-

*These authors contributed equally to this work.

†Contact author: maximilian.zawierucha@ptb.de, he/him/his

‡Contact author: fabian.wolf@ptb.de, he/him/his

Published by the American Physical Society under the terms of the [Creative Commons Attribution 4.0 International license](https://creativecommons.org/licenses/by/4.0/). Further distribution of this work must maintain attribution to the author(s) and the published article's title, journal citation, and DOI.

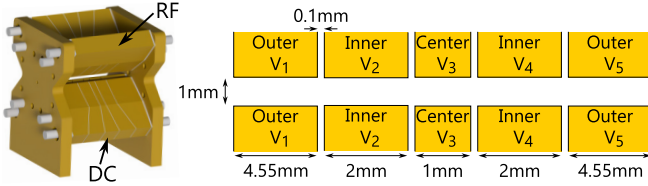


FIG. 1. Ion-trap geometry. Left: CAD render of the ion trap used in the described experiments. It is constructed using gold-coated alumina pieces. Segmentation of dc electrodes is achieved by laser cutting. The top right and bottom left blades carry a rf signal at 23.456 MHz for radial confinement of the ions. The other two blades carry adjustable dc electric potentials for axial confinement of the ions and for performing ion-chain shuttling and splitting operations. Right: Nomenclature and sizes of the dc segments.

ing selected ions. In addition to the improved robustness of these schemes, large crystals of laser-cooled ions provide faster sympathetic cooling for cotrapped species that cannot be laser cooled directly. Crystallization times decrease with $1/n$, where n is the number of coolant ions [29]. Therefore, a higher number of coolant ions circumvents the problem of long crystallization times of up to 18 min, which have been observed, for example, in aluminum quantum logic clocks [29,38,57] or recapture of highly charged ions [58]. These long crystallization times can render additive schemes impractical.

In previously demonstrated subtractive schemes [59–61], the removed ions were selected by their charge-to-mass ratio, making it difficult to control the exact number of remaining ions. Furthermore, it is challenging to individually remove ion species with a similar charge-to-mass ratio. These methods can be very fast, on the order of ~ 5 ms [61]; however, very careful tuning of ejection parameters is needed.

Unlike previously demonstrated methods, the ejection approach presented here is independent of the ion species being removed. Notably, the presented method is also applicable when both species have the same (or similar) charge-to-mass ratio, which is of particular importance for the investigation of multiply charged or molecular ions. As a result, this approach offers the capability to generate dual-species ion crystals with arbitrary composition. An extension to multispecies ion crystals is possible if the composition of the ensemble can be determined.

II. EXPERIMENTAL SETUP

The experiment at hand is a trapped-ion spectroscopy setup. We use a linear Paul trap for trapping ions at ultrahigh vacuum ($<10^{-10}$ mbar). A computer-aided-design (CAD) render of the trap is given in Fig. 1. The distance between electrodes and the ions is 0.5 mm. The two opposing dc blades are segmented into five electrodes each, which can be individually addressed to provide axial confinement. With these segments, a double-well potential, resulting in two axially separated trapping regions, can be realized. A more detailed description of a similar trap and its construction can be found in [62]. The experiments described here were performed with $^{40}\text{Ca}^+$ and $^{25}\text{Mg}^+$ ions. The calcium ions are laser cooled with light at 397 nm. The resulting fluorescence of the ions is imaged

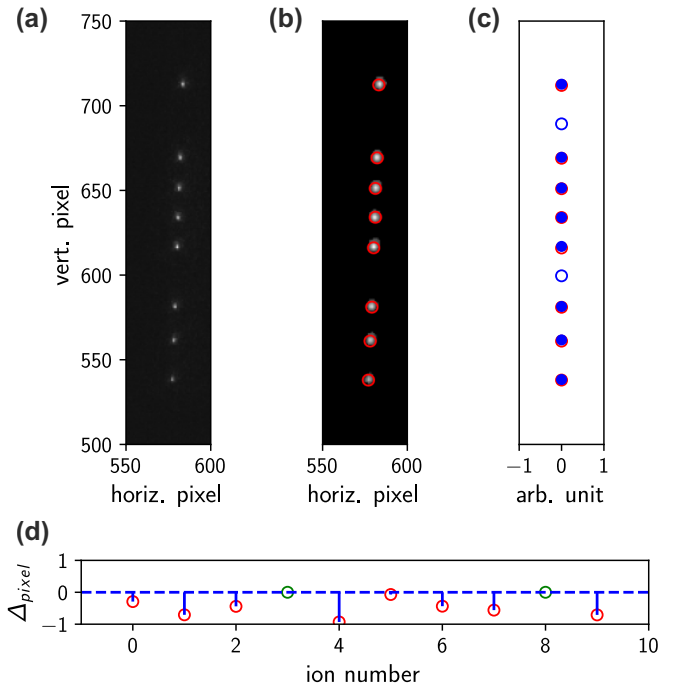


FIG. 2. Step-by-step illustration of the ion-chain detection process. (a) Unprocessed image of the ion chain taken with the EMCCD camera. (b) Applied Gauss and Otsu filters and a peak detector to find the ion positions. Red circles visualize bright calcium ions detected by the algorithm. (c) Result of the dark-ion detection. Empty circles indicate dark-ion positions. The eight previously detected bright ions are indicated by filled circles. (d) Deviation of the detected ion positions from the best matching calculated ion chain.

on an electron-multiplying CCD (EMCCD) camera using a single aspheric lens. The magnesium ions are not directly laser cooled and are not detected via fluorescence imaging. They appear as dark defects in the Coulomb crystal and act as a placeholder for other species for which fluorescence detection is not feasible.

Both ion species are loaded via ablation loading with a matchbox-sized laser at 515 nm (Mountain Photonics GmbH, IOP 0515L-21C-NI-NT-NF). The laser is pulsed with a repetition rate of 3.5 kHz and provides pulse powers of approximately $30 \mu\text{J}$. It can either be focused onto a calcium or magnesium target inside the vacuum chamber, using a motorized mirror. The ablated calcium ions are photoionized, resembling the scheme described in [63]. Magnesium-25 is loaded from an enriched target without an ionization laser, similar to experiments with other species [56].

After ion loading, the trapping parameters fulfill $\omega_{x,y} \gg \omega_z$, where $\omega_{x,y}$ and ω_z are the radial and axial trap frequencies of a single trapped ion, respectively. In our case these values are $\omega_x = 2\pi \times 750$ kHz, $\omega_y = 2\pi \times 950$ kHz, and $\omega_z = 2\pi \times 143$ kHz. This configuration results in the ions aligning in a linear chain along the axial trap direction (see Fig. 2).

III. ION DETECTION

To determine the composition of a dual-species crystal containing calcium and magnesium ions, two detection steps are

required. For laser-cooled calcium ions the employed imaging system resolves the individual ions, which are typically separated by a few micrometers for the used trap settings [see Fig. 2(a)]. Therefore, the calcium ions' positions can be extracted by detecting fluorescence peaks in the camera image. These measured positions are compared to precalculated theoretical values [64] for ion crystals of different sizes, revealing information about the number of nonfluorescing magnesium ions present in the crystal. This process is discussed in detail in the following sections.

A. Bright-ion detection

To detect the bright calcium ions' positions and quantity, an image is taken using an EMCCD camera with a 14-bit brightness resolution and an exposure time of 0.2 s [see Fig. 2(a)]. The image quality is compromised by noise, predominantly electronic noise, background photons, and defective (bright) pixels. In order to mitigate this noise, the image is postprocessed. False ion detections due to single bright pixels are effectively suppressed by applying a Gaussian filter with a width of 1 pixel and setting pixels below a certain threshold to zero brightness.

A good initial guess for this threshold is provided by the "Otsu" threshold determination method [65]. Afterwards, a peak detection function is used to determine the bright ions' positions with a resolution of 1 pixel. More details and the specific functions used can be found in Appendix B.

The bright-ion detection works well for linear ion chains and slight-zigzag configurations with up to approximately 20 ions. An example of this process can be found in Fig. 2(b).

B. Dark-ion detection

In the experiments described here, magnesium ions are not directly laser cooled and are not detected via fluorescence imaging. However, when the bright calcium ions' positions are determined, the dark magnesium ions' quantity and location in the crystal can be inferred. This is done by comparing precalculated equilibrium positions to the detected positions of the calcium ions. A similar method was used to count ions in a long chain, where only the central part of the chain was imaged [66].

Since the ion chain is mostly aligned along the vertical camera axis, we consider only the ions' vertical position component. More information on this can be found in Appendix A.

The equilibrium positions of ions in a linear chain are calculated following [64]. In order to map the calculated ion positions to an expected pixel position on the camera P_j^{theo} , a calibration is needed, as described in Appendix A.

The total number of bright and dark ions n is determined by minimizing the measure $b(n)$, defined as

$$b(n) = \sum_i \frac{\min_j |P_i - P_j^{\text{theo}}(n)|^2}{n_{\text{bright}}}, \quad (1)$$

which is the mean distance of the measured ion positions P_i of the fluorescing ions to the closest theoretically determined position $P_j^{\text{theo}}(n)$. n_{bright} is the number of fluorescing ions, determined by the previously described measurement. The number of dark ions n_{dark} is determined by subtracting n_{bright}

from n . For the minimization of $b(n)$, the total number of ions was limited to $n < \min(2n_{\text{bright}}, 23)$. This choice helps to mitigate detection errors as described in Sec. III C. The normalization of $b(n)$ to the number of bright ions is analogous to a reduced- χ^2 analysis and allows comparing the quality of the fit between crystals of different sizes.

The result of such a dark-ion-position determination is given in Fig. 2(c), with a typical deviation between detected and calculated ion positions below 1 pixel [see Fig. 2(d)].

C. Benchmark and limitation

In order to benchmark the performance of the dark-ion-detection scheme, it was run on a dataset with a sample size of 205 456. The data were generated by recording ion chains with lengths of up to 10 fluorescing ions. The previously described process was used to infer the camera position P_i of the fluorescing ions. Dual-species ion chains were simulated by selectively removing position data from the purely bright dataset. The dark-ion-detection algorithm was used to predict the ion-chain configuration. In this implementation of the detection algorithm a maximum number of 20 ions was assumed. Figure 3(a) illustrates the detection error for different ratios of dark and bright ions. Each scatter represents one particular configuration of ions. Configurations with a larger fraction of dark to bright ions are more prone to detection errors. Also, configurations with $n_{\text{bright}} > n_{\text{dark}}$ can be detected incorrectly. These false detections are caused by falsely assuming an ion chain with $n_{\text{bright}} < n_{\text{dark}}$. The resulting errors can be mitigated by restricting the theoretical configurations that are compared to the bright-ion positions to configurations with $n'_{\text{bright}} \geq n'_{\text{dark}}$. When describing restrictions for the detection algorithm, a prime (') is added to the ion number. Figure 3 shows that this restriction suppresses errors entirely for configurations with $n_{\text{bright}} \geq n_{\text{dark}}$ at the cost of restricting the detection algorithm to this subset of configurations. Experimentally, this precondition can be easily met by an appropriate choice of loading parameters. The condition $n'_{\text{bright}} \geq n'_{\text{dark}}$ can be generalized by introducing the limiting ratio $n'_{\text{bright}}/n'_{\text{dark}}$. The previously described precondition corresponds to $n'_{\text{bright}}/n'_{\text{dark}} \geq 1$. Figure 3(c) shows the detection-error dependence of the limiting ratio and illustrates the trade-off between a low average detection error and a large number of detectable configurations. In all experiments described here, a limiting ratio of $n'_{\text{bright}}/n'_{\text{dark}} = 1$ was used. More details regarding the origin of the detection errors can be found in Appendix D.

Additionally, there are technical limitations of the detection scheme, restricting its application to 23 ions with the parameters used. Larger ion numbers lead to the formation of three-dimensional (3D) crystals for the chosen trapping parameters. These structures cannot be interpreted by our detection method. To align larger ion crystals linearly, a higher radial confinement is necessary, which is infeasible in our setup. In general, increasing the ion number increases the ion density in the center of the trap for a given axial confinement. Therefore, it becomes more difficult to distinguish between ion chains with similar ion numbers. Overcoming this limitation would require higher spatial resolution of the imaging system or operating at a lower axial confinement to get a larger

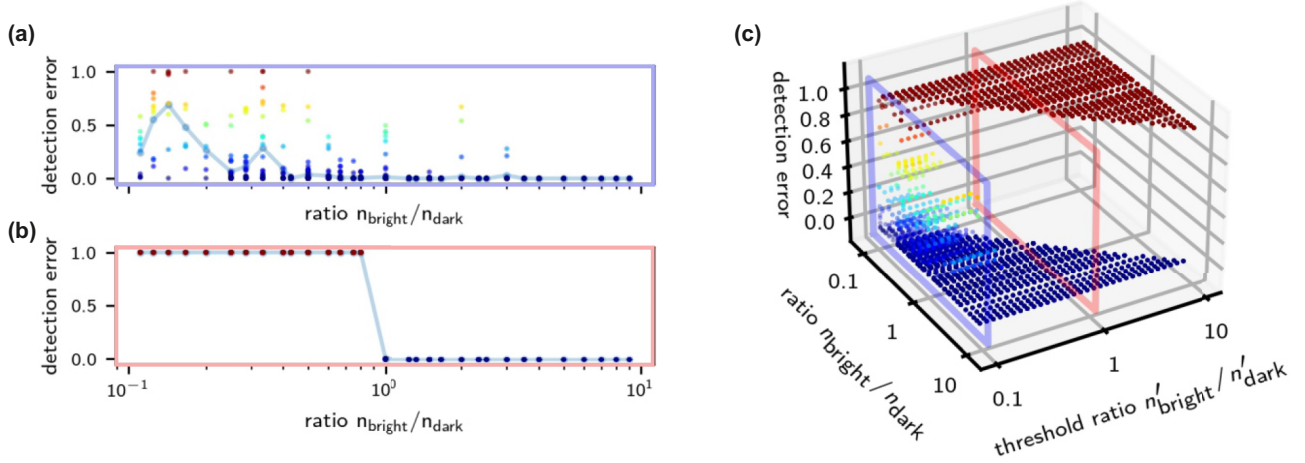


FIG. 3. Simulated detection error for ion crystals with $n \leq 10$ for different ratios between dark and bright ions. (a) The detection error for arbitrary ion configurations with $n' \leq 20$ compared to the detected bright-ion positions. Each scatter corresponds to one ion-chain configuration. The blue line denotes the average detection error for a given bright to dark ion ratio. (b) The detection error with the additional restriction for the reference positions that more bright ions than dark ions are in the ion chain. (c) The general case for different threshold ratios between dark and bright ions in the reference configurations. See text for additional information.

separation of the ions. The implementation presented here determines only the ions position P_i with 1 pixel resolution. More advanced peak detection methods could be used to interpolate the region between camera pixels, thereby providing higher resolution. Decreasing the axial potential has its limits, as a very low axial confinement leads to fluctuating ion positions because the position becomes much more sensitive to external electric-field perturbations. Also, increasingly larger ion chains may no longer be within the detection region.

IV. ION OPERATIONS

The presented ion-crystal-preparation procedure relies on splitting an ion chain into two parts and discarding the side which is farther from a desired target crystal. The decision logic is depicted in Table I. In total, four different operations on the ion crystal are required: (1) splitting the ion chain into two subchains, (2) shuttling a subchain into the detection region, (3) determination of the composition of an ion chain, and (4) selectively discarding one of the subchains (left or right). These operations are implemented by applying different sets of voltages to the individual dc electrodes, realizing the required potential landscapes. The applied voltages in our realization of this method are shown in Fig. 4.

For the splitting operations, the ions are initially confined in a shallow potential ($\omega_z = 2\pi \times 143$ kHz), and the voltage on the center electrode (V_3) is gradually increased, forming a double-well potential that splits the ion chain in two parts. The nomenclature for the blade segments is given in Fig. 1. The ratio of ions in the left and right wells of the potential can be controlled by shifting the equilibrium position of the ions in the axial direction before splitting. This is done by applying an additional differential voltage ΔU to the outer electrodes (V_1 and V_5). A measurement of the dependence of the splitting ratio on the differential voltage is shown in Fig. 5. From these measurements, ΔU can be set such that the ion crystal is split in half. More details can be found in

Appendix C. This splitting ratio voltage is applied to all ion operations.

The minima of the double-well potential formed at the end of the splitting operation are outside of our imaging region. Therefore, to determine the constituents, a shuttling operation is required to move one of the subchains back while keeping both parts separated. This is achieved by increasing the outer electrodes' voltage on one of the sides, V_1 or V_5 , and applying a small trapping potential to the inner electrodes (V_2 and V_4).

When one of the subchains is shuttled into the imaging region, the other subchain is trapped in the region of the outer electrode. There, confinement in the axial direction is partially provided by the voltage on electrode V_4 or V_2 and the axial component of the rf potential in the outer region of the trap.

TABLE I. Decision process for discarding one side of the ion chain after the split.

| Step | Condition | Action | |
|------|--|---|---------------|
| 1 | $n_{\text{bright}} \geq n_{\text{dark}} > 0$ | | |
| | Left, right | | |
| | False, false | | Error |
| | False, true | | Discard left |
| | True, false | | Discard right |
| 2 | True, true | Continue | |
| | $n_{\text{dark}}^{\text{left}} > n_{\text{dark}}^{\text{right}}$ | Discard left | |
| | $n_{\text{dark}}^{\text{left}} < n_{\text{dark}}^{\text{right}}$ | Discard right | |
| 3 | $n_{\text{dark}}^{\text{left}} = n_{\text{dark}}^{\text{right}}$ | Continue | |
| | $n_{\text{bright}}^{\text{left}} > n_{\text{bright}}^{\text{right}}$ | Discard right | |
| | $n_{\text{bright}}^{\text{left}} < n_{\text{bright}}^{\text{right}}$ | Discard left | |
| | $n_{\text{bright}}^{\text{left}} = n_{\text{bright}}^{\text{right}}$ | Discard either side; we discard left | |

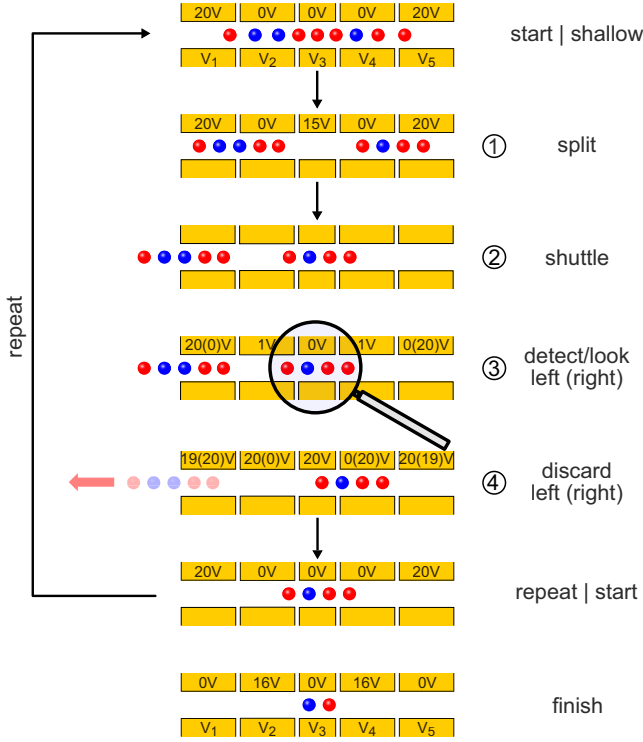


FIG. 4. Visualization of an automated two-ion-crystal production loop. Blue and red balls depict the different ion species. Note that the ion position and distance with respect to the depicted segments is not to scale.

The last required operation is the ejection of the unwanted subchain from the trap. This operation is implemented by increasing the center voltage to 20 V (V_3). The voltages on the side where the ions should be discarded are set to 19 V on the outer segment (V_1 or V_5) and 20 V on the inner segment (V_2 or V_4). These voltages are needed to overcome the residual rf confinement in the axial direction. In order to keep the other subchain of ions trapped, the voltages are modified to 0 V (V_4 or V_2) on the inner segment and 20 V on the outer segment (V_5 or V_1).

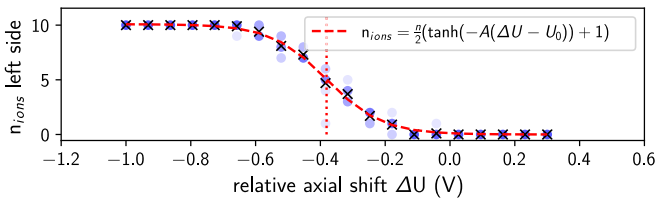


FIG. 5. Calibration of the splitting process. A 10-ion crystal was split, and the ions on the left side were counted. The measurement was repeated 10 times for each value of ΔU . The crosses denote the average ion number detected on the left side. The circles show each measurement result, with the frequency encoded in the visibility of the circle. The red dashed line shows a fit to the data, which is used to infer the voltage U_0 needed to split the crystal into equal parts, shown by the dotted line.

V. AUTOMATION

Combining the previously discussed operations with the ion-detection protocol allows us to automate the process for dual-species two-ion preparation. Our implementation of this automation was integrated into the Advanced Real-Time Infrastructure for Quantum physics (ARTIQ) framework [67].

A. Ion preparation scheme

The automated two-ion-crystal preparation starts by loading a dual-species ion chain. We select the loading parameters such that the number of bright ions is larger than the number of dark ions, i.e., $n_{\text{bright}} \geq n_{\text{dark}} > 0$. Fulfilling this condition prevents errors in the dark-ion detection (see Sec. III C) and results in more efficient cooling of the ions.

After checking that $n_{\text{bright}} > 0$ and $n_{\text{dark}} > 0$, the main loop for the preparation algorithm starts. First, the ion chain is split into two subchains of similar size. Both subchains are subsequently shuttled to the center segment to determine their constituents. Afterwards, one of the subchains is ejected, with the specific subchain determined based on the logical pathway depicted in Table I. Then the loop starts again with the remaining ions. The algorithm is visualized in Fig. 4.

The decision regarding which side to discard is made according to the following logic: First, we check whether either of the two subchains fulfills the “start condition” (see above). If that is not the case, the ion chains are merged, and the loop is restarted. If only one of the two subchains fulfills the start condition, that subchain is kept, the other one is discarded, and the loop is restarted. If both subchains fulfill the start condition, additional decision factors are taken into account. First, the number of dark ions are compared. The subchain with fewer dark ions is kept, while the other one is discarded since fewer dark ions are beneficial for the cooling performance. If the subchains do not differ in this parameter, the one with more bright ions is kept. If the subchains are identical, the left subchain is discarded, with the selection being arbitrary. This decision process is summarized in Table I.

This loop is repeated until a two-ion crystal with exactly one dark ion and one bright ion is left.

In addition, we have implemented a verification to determine whether the detection worked as expected. If the number of detected bright and dark ions before splitting does not match the number of bright and dark ions detected after the split, the subchains are remerged, and the loop is restarted. If the starting condition is no longer fulfilled at the beginning of the loop, the algorithm will stop and raise an error.

B. Experimental results

The algorithm described above was run starting from 100 ion chains containing 10 to 20 ions. Each initial ion configuration was successfully reduced to a dual-species two-ion ion chain.

The reported samples showed no instances where the algorithm failed. It typically took around four splitting operations to arrive at the final ion chain. This translates to a time of ~ 80 s in our setup. The runtime is mainly determined by the conservative waiting time of 18 s per splitting cycle to make sure that the ion chain is crystallized. Figure 6 shows

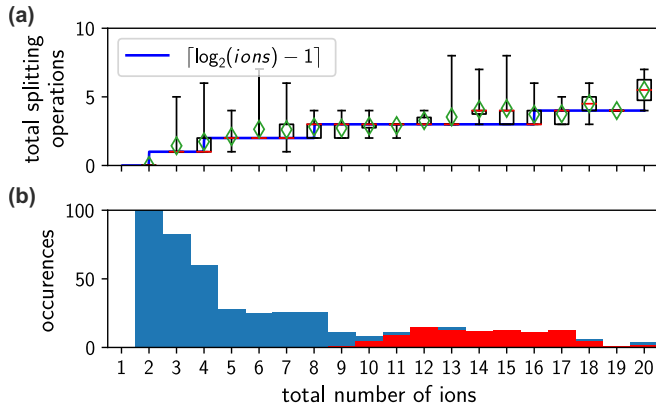


FIG. 6. Performance of the two-ion crystal distillation. (a) The number of splitting operations needed to reduce a given ion crystal to a two-ion crystal. Visualization is done via a box plot due to the asymmetric error distribution. The whiskers show the min and max values, while the box extends from the first quartile to the third quartile. The red lines indicate the median, and the green diamonds mark the average of the distribution. The blue curve shows the expected scaling of the algorithm. (b) Histogram of the ion-number occurrences during the data taking. The histogram gives the sample size for each data point in the plot above; 100 dual-species ion-crystal chains were prepared with ion numbers between 10 and 20 (red bars) and reduced to a two-ion crystal using the described algorithm. The blue bars show the intermediate ion crystal sizes.

the number of split operations needed to arrive at a two-ion crystal, depending on the size of the initial ion-crystal configuration. During the procedure of forming a two-ion crystal, the algorithm naturally produces ion chains which are smaller than the starting size. These intermediate ion chains were all tracked and interpreted as start configurations. Therefore, smaller starting ion-chain configurations could be analyzed without producing them by ion loading. With this procedure we could generate around 300 data points from 100 prepared ion crystals.

For a process that ideally splits the ion chain in the center, one would expect the number of splitting operations to follow $\lceil \log_2(n) - 1 \rceil$, with n being the total number of ions. Since only integer values of splitting operations are possible, the ceiling function ($\lceil \cdot \rceil$) is needed. This estimate is indicated by the blue line in Fig. 6. Most median values follow that expected curve.

VI. OUTLOOK

The presented scheme of ion-crystal preparation can be extended to produce ion crystals with an arbitrary dual-species ion composition, as long as the compositions of the subchains can be determined. This could be achieved by changing the decision tree or by changing the splitting ratio dynamically. Before each split operation, an optimal splitting ratio could be determined and used in order to prepare the desired ion-crystal composition, possibly combined with ion reordering [68]. A dynamic splitting ratio would also increase the speed of the algorithm.

The algorithm runtime is limited by very conservative waiting times to ensure the ion chains are crystallized after each

step. With state-of-the-art ion splitting and shuttling operations [69–71], ions can be moved quickly while introducing only a small amount of heating. Data handling and detection times can also be improved, as shown in [72–74]. Combining these techniques, the algorithm’s speed could be improved to reach millisecond timescales.

In the work presented here, only ion crystals up to 20 ions were investigated. Extending the procedure to larger numbers of ions is possible, as the algorithm runtime scales very favorably (logarithmic) with ion number. For larger ion chains the axial trapping potential would need to be lowered, or the radial confinement would need to be increased. Alternatively, a more involved detection scheme capable of calculating and detecting ion positions in a 3D crystal could be implemented [75].

VII. CONCLUSION

We presented a simple, deterministic, and efficient technique for preparing a dual-species, two-ion crystal from a large dual-species ion crystal and demonstrated an automated implementation. The method at hand produces a two-ion crystal in less than 2 min. It alleviates the need for fine tuning of loading parameters, which increases the robustness and reproducibility of preparing dual-species two-ion crystals. Our method is easily extendable to produce different configurations of dual-species ion crystals and can be further optimized for speed. The presented scheme relies on experimental techniques that are available in quantum CCD architectures for quantum computing [76,77] and are well suited for trapped ion quantum technology due to the demonstrated high level of automation.

ACKNOWLEDGMENTS

We want to thank J. Kiethe and E. Surzhikova for developing and providing the readout script for the EMCCD camera which was used in this work. We acknowledge additional dark-ion-detection insights from L. Schomburg and T. Nordmann. Additionally, we thank L. Spieß for careful reading of the manuscript and for providing valuable suggestions and K. Dietze for helpful support with the ARTIQ experimental control. This research was funded by the Deutsche Forschungsgemeinschaft (DFG, German Research Foundation), Project ID No. 274200144, SFB 1227 (DQ-mat), Projects No. B05 and No. B03 with partial support from Germany’s Excellence Strategy EXC-2123 QuantumFrontiers 390837967. This project received funding from the European Research Council (ERC) under the European Union’s Horizon 2020 research and innovation program (Grant Agreement No. 101019987). This work was partially funded by 22IEM01 TOCK and received support from the Max Planck-RIKEN-PTB Center for Time Constants and Fundamental Symmetries. The project (22IEM01 TOCK) has received funding from the European Partnership on Metrology, cofinanced from the European Union’s Horizon Europe Research and Innovation Programme and by the Participating States.

T.R., M.J.Z., and F.W. conceived the main idea of this research and carried out the experiments. Furthermore, T.R., M.J.Z., P.O.S., and F.W. advanced the work by interpreting

the results, steering the research, and writing the manuscript. J.K. and T.E.M. contributed the idea of the dark-ion-detection principle and proved its usefulness in another experimental setup.

APPENDIX A: TRANSFORMATION FROM CALCULATED ION POSITIONS TO CAMERA PIXELS

The theoretically determined position of the j th ion with respect to the center of the ion chain is given by $x'_j = lu_j$, where u_j is the dimensionless equilibrium position that can be computed analytically for two and three ions and needs to be calculated numerically for larger ion chains [64]. The length scale l for singly ionized ions is given by

$$l^3 = \frac{e^2}{4\pi\epsilon_0 C_{\text{trap}} U_{\text{dc}}}, \quad (\text{A1})$$

where e is the charge of the electron, ϵ_0 is the permittivity of free space, C_{trap} is a constant given by the geometry of the ion trap, and U_{dc} is the voltage that provides the axial confinement.

The position of the image on the camera P_j^{theo} is related to the ion's position u_j by $P_j^{\text{theo}} = P_0 + Ku_j$, where P_0 denotes the center of the ion chain on the camera chip and $K = lM/s_{\text{px}}$ is a factor that accounts for the magnification factor M of the imaging system and the pixel size s_{px} . The values for P_0 and K are inferred from loading a known number of fluorescing ions (≥ 2) and determining their position on the camera image.

An angle of $\alpha \approx 2^\circ$ between the ion-chain axis and the camera axis leads to a linear rescaling of the ion distances. However, these changes in ion distances are below the ion-detection resolution and get absorbed in the calibration process.

APPENDIX B: BRIGHT-ION-DETECTION DETAILS

Determining the threshold in the bright-ion detection is done by the Otsu threshold determination from the PYTHON SCIKIT-IMAGE module (`skimage.filters.threshold_otsu`, V0.20.0 [78]). Lower detection errors are obtained by increasing this resulting threshold by 200 (out of the full dynamic range of 14 bits), which was determined in a heuristic approach. A detailed description of the Otsu threshold determination can be found in Ref. [65]. A peak detection function (`skimage.feature.peak_local_max` [78]) from SCIKIT-IMAGE is used to determine the bright ions' positions with a resolution of 1 pixel. To avoid double counting of single ions, we chose a minimum distance of 6 pixels ($\sim 4 \mu\text{m}$) between detected ion positions.

APPENDIX C: SPLIT RATIO CALIBRATION

Measuring the number of ions on one side of the double-well potential for different differential voltages ΔU between electrodes V_1 and V_5 and fitting a model to the data allow us to find a value for ΔU matching the desired splitting ratio. Here we are interested in a splitting ratio of 1.

The number of ions in the left well after the split resembles the heuristic function

$$n_{\text{left}}(\Delta U) = \frac{n}{2} \tanh[-A(\Delta U - \Delta U_0) + 1], \quad (\text{C1})$$

where n is the total number of ions, A is a scaling factor, and ΔU_0 is the differential voltage, for which the ion crystal is split in half. A fit of (C1) to measured data is shown in Fig. 5.

APPENDIX D: DETECTION ERRORS

When detecting the ion-chain configuration, errors can occur if there is no limit to the number of dark ions. Most of these errors originate in ion-chain configurations for which some ion positions are similar for different configurations. In this context, "similar" means that the position cannot be differentiated with the given experimental position resolution. If only these similar ion positions are occupied by bright ions, the different configurations are indistinguishable to the algorithm. For large ion crystals the density of ions increases, and therefore, those ion chains often have a subset of ion positions which are almost identical to some ion positions of a smaller ion crystal. The most obvious example of a position which is similar in many ion chains is the center position in an odd-numbered ion crystal. If only one fluorescing ion is trapped, it is impossible to determine the total chain size since nonfluorescing ions could be present and located on each side of the bright central ion. An illustration of a typical false detection can be found in Fig. 7.

These errors can be mitigated by limiting the allowed ion-chain configurations to ones with $n'_{\text{bright}} \geq n'_{\text{dark}}$ or by a more accurate bright-ion-position determination (this would, however, not solve the problem with only one fluorescing ion in the center).

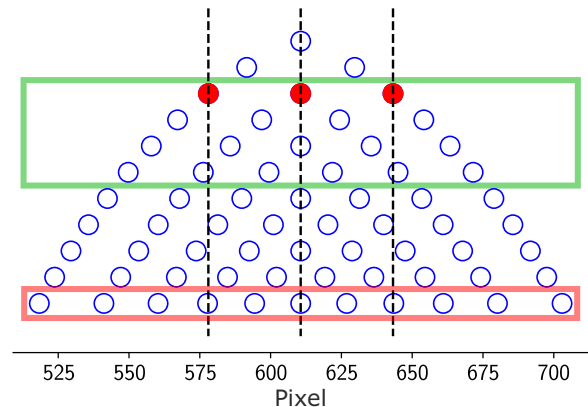


FIG. 7. Example of configurations that are difficult to distinguish. Shown are calculated ion positions for ion chains with ion numbers between 1 and 11. Circles illustrate ion positions. Assuming three trapped bright ions (red circles), there is a configuration with 11 ions which includes three ion positions almost matching the positions of the three trapped ions. The green rectangle marks the region of interest for our dark-ion-detection scheme, applying the limiting ratio of $n'_{\text{dark}}/n'_{\text{bright}} = 1$. The black lines mark the positions of the three bright ions. Without the limiting ratio, the dark-ion-detection scheme cannot reliably distinguish between the three-bright-ion configuration and the 11-ion configuration marked in red with three bright ions located at the same locations as the ions in the three-ion crystal and eight dark ions.

- [1] A. D. Ludlow, M. M. Boyd, J. Ye, E. Peik, and P. O. Schmidt, *Rev. Mod. Phys.* **87**, 637 (2015).
- [2] S. M. Brewer, J.-S. Chen, A. M. Hankin, E. R. Clements, C. W. Chou, D. J. Wineland, D. B. Hume, and D. R. Leibbrandt, *Phys. Rev. Lett.* **123**, 033201 (2019).
- [3] N. Huntemann, C. Sanner, B. Lipphardt, C. Tamm, and E. Peik, *Phys. Rev. Lett.* **116**, 063001 (2016).
- [4] Z. Zhiqiang, K. J. Arnold, R. Kaewuam, and M. D. Barrett, *Sci. Adv.* **9**, eadg1971 (2023).
- [5] Y. Huang, B. Zhang, M. Zeng, Y. Hao, Z. Ma, H. Zhang, H. Guan, Z. Chen, M. Wang, and K. Gao, *Phys. Rev. Appl.* **17**, 034041 (2022).
- [6] M. Brownnutt, M. Kumph, P. Rabl, and R. Blatt, *Rev. Mod. Phys.* **87**, 1419 (2015).
- [7] F. Wolf, C. Shi, J. C. Heip, M. Gessner, L. Pezzè, A. Smerzi, M. Schulte, K. Hammerer, and P. O. Schmidt, *Nat. Commun.* **10**, 2929 (2019).
- [8] W. C. Campbell and P. Hamilton, *J. Phys. B* **50**, 064002 (2017).
- [9] I. Baumgart, J.-M. Cai, A. Retzker, M. B. Plenio, and C. Wunderlich, *Phys. Rev. Lett.* **116**, 240801 (2016).
- [10] K. A. Gilmore, M. Affolter, R. J. Lewis-Swan, D. Barberena, E. Jordan, A. M. Rey, and J. J. Bollinger, *Science* **373**, 673 (2021).
- [11] M. J. Biercuk, H. Uys, J. W. Britton, A. P. VanDevender, and J. J. Bollinger, *Nat. Nanotechnol.* **5**, 646 (2010).
- [12] K. C. McCormick, J. Keller, S. C. Burd, D. J. Wineland, A. C. Wilson, and D. Leibfried, *Nature (London)* **572**, 86 (2019).
- [13] J. I. Cirac and P. Zoller, *Phys. Rev. Lett.* **74**, 4091 (1995).
- [14] R. Blatt and D. Wineland, *Nature (London)* **453**, 1008 (2008).
- [15] C. D. Bruzewicz, J. Chiaverini, R. McConnell, and J. M. Sage, *Appl. Phys. Rev.* **6**, 021314 (2019).
- [16] M. D. Barrett, K. J. Arnold, and M. S. Safronova, *Phys. Rev. A* **100**, 043418 (2019).
- [17] F. Wolf, *Phys. Rev. Lett.* **132**, 083202 (2024).
- [18] M. Steinel, H. Shao, M. Filzinger, B. Lipphardt, M. Brinkmann, A. Didier, T. E. Mehlstäubler, T. Lindvall, E. Peik, and N. Huntemann, *Phys. Rev. Lett.* **131**, 083002 (2023).
- [19] J. B. Wübbena, S. Amairi, O. Mandel, and P. O. Schmidt, *Phys. Rev. A* **85**, 043412 (2012).
- [20] S. A. King, L. J. Spieß, P. Micke, A. Wilzewski, T. Leopold, J. R. Crespo López-Urrutia, and P. O. Schmidt, *Phys. Rev. X* **11**, 041049 (2021).
- [21] R. Rugango, J. E. Goeders, T. H. Dixon, J. M. Gray, N. B. Khanyile, G. Shu, R. J. Clark, and K. R. Brown, *New J. Phys.* **17**, 035009 (2015).
- [22] Y. Wan, F. Gebert, F. Wolf, and P. O. Schmidt, *Phys. Rev. A* **91**, 043425 (2015).
- [23] S. Sels, F. M. Maier, M. Au, P. Fischer, C. Kanitz, V. Lagaki, S. Lechner, E. Leistschneider, D. Leimbach, E. M. Lykiardopoulou, A. A. Kwiatkowski, T. Manovitz, Y. N. Vila Gracia, G. Neyens, P. Plattner, S. Rothe, L. Schweikhard, M. Vilen, R. N. Wolf, and S. Malbrunot-Ettenauer, *Phys. Rev. Res.* **4**, 033229 (2022).
- [24] T. Meiners, M. Niemann, J. Mielke, M. Borchert, N. Pulido, J. M. Cornejo, S. Ulmer, and C. Ospelkaus, *Hyperfine Interact.* **239**, 26 (2018).
- [25] K.-F. Cui, J.-J. Shang, S.-J. Chao, S.-M. Wang, J.-B. Yuan, P. Zhang, J. Cao, H.-L. Shu, and X.-R. Huang, *J. Phys. B* **51**, 045502 (2018).
- [26] A. T. Calvin, S. Janardan, J. Condoluci, R. Rugango, E. Pretzsch, G. Shu, and K. R. Brown, *J. Phys. Chem. A* **122**, 3177 (2018).
- [27] N. Ohtsubo, Y. Li, K. Matsubara, T. Ido, and K. Hayasaka, *Opt. Express* **25**, 11725 (2017).
- [28] J.-S. Chen, S. M. Brewer, C. W. Chou, D. J. Wineland, D. R. Leibbrandt, and D. B. Hume, *Phys. Rev. Lett.* **118**, 053002 (2017).
- [29] M. Guggemos, D. Heinrich, O. A. Herrera-Sancho, R. Blatt, and C. F. Roos, *New J. Phys.* **17**, 103001 (2015).
- [30] S. Willitsch, M. T. Bell, A. D. Gingell, and T. P. Softley, *Phys. Chem. Chem. Phys.* **10**, 7200 (2008).
- [31] T. Kwapien, U. Eichmann, and W. Sandner, *Phys. Rev. A* **75**, 063418 (2007).
- [32] V. L. Ryjkov, X. Z. Zhao, and H. A. Schuessler, *Phys. Rev. A* **74**, 023401 (2006).
- [33] A. Ostendorf, C. B. Zhang, M. A. Wilson, D. Offenbergh, B. Roth, and S. Schiller, *Phys. Rev. Lett.* **97**, 243005 (2006).
- [34] B. Roth, U. Fröhlich, and S. Schiller, *Phys. Rev. Lett.* **94**, 053001 (2005).
- [35] P. O. Schmidt, T. Rosenband, C. Langer, W. M. Itano, J. C. Bergquist, and D. J. Wineland, *Science* **309**, 749 (2005).
- [36] K. Cui, S. Chao, C. Sun, S. Wang, P. Zhang, Y. Wei, J. Yuan, J. Cao, H. Shu, and X. Huang, *Eur. Phys. J. D* **76**, 140 (2022).
- [37] M. Guggemos, M. Guevara-Bertsch, D. Heinrich, O. A. Herrera-Sancho, Y. Colombe, R. Blatt, and C. F. Roos, *New J. Phys.* **21**, 103003 (2019).
- [38] J. A. Kramer, Ph.D. thesis, *Gottfried Wilhelm Leibniz Universität*, 2023.
- [39] P. Micke, T. Leopold, S. A. King, E. Benkler, L. J. Spieß, L. Schmöger, M. Schwarz, J. R. C. López-Urrutia, and P. O. Schmidt, *Nature (London)* **578**, 60 (2020).
- [40] S. A. King, L. J. Spieß, P. Micke, A. Wilzewski, T. Leopold, E. Benkler, R. Lange, N. Huntemann, A. Surzhykov, V. A. Yerokhin, J. R. Crespo López-Urrutia, and P. O. Schmidt, *Nature (London)* **611**, 43 (2022).
- [41] C. W. Chou, A. L. Collopy, C. Kurz, Y. Lin, M. E. Harding, P. N. Plessow, T. Fortier, S. Diddams, D. Leibfried, and D. R. Leibbrandt, *Science* **367**, 1458 (2020).
- [42] F. Wolf, Y. Wan, J. C. Heip, F. Gebert, C. Shi, and P. O. Schmidt, *Nature (London)* **530**, 457 (2016).
- [43] Y. Wang, M. Um, J. Zhang, S. An, M. Lyu, J.-N. Zhang, L.-M. Duan, D. Yum, and K. Kim, *Nat. Photonics* **11**, 646 (2017).
- [44] P. Wang, C.-Y. Luan, M. Qiao, M. Um, J. Zhang, Y. Wang, X. Yuan, M. Gu, J. Zhang, and K. Kim, *Nat. Commun.* **12**, 233 (2021).
- [45] T. G. Ballance, J. F. Goodwin, B. Nichol, L. J. Stephenson, C. J. Ballance, and D. M. Lucas, *Rev. Sci. Instrum.* **89**, 053102 (2018).
- [46] S. Gao, W. J. Hughes, D. M. Lucas, T. G. Ballance, and J. F. Goodwin, *Rev. Sci. Instrum.* **92**, 033205 (2021).
- [47] J. M. Sage, A. J. Kerman, and J. Chiaverini, *Phys. Rev. A* **86**, 013417 (2012).
- [48] C. D. Bruzewicz, R. McConnell, J. Chiaverini, and J. M. Sage, *Nat. Commun.* **7**, 13005 (2016).
- [49] D. R. Leibbrandt, R. J. Clark, J. Labaziewicz, P. Antohi, W. Bakr, K. R. Brown, and I. L. Chuang, *Phys. Rev. A* **76**, 055403 (2007).
- [50] Q. Wu, M. Filzinger, Y. Shi, Z. Wang, and J. Zhang, *Rev. Sci. Instrum.* **92**, 063201 (2021).

- [51] X. Shi, S. L. Todaro, G. L. Mintzer, C. D. Bruzewicz, J. Chiaverini, and I. L. Chuang, *Appl. Phys. Lett.* **122**, 264002 (2023).
- [52] B. M. White, P. J. Low, Y. de Sereville, M. L. Day, N. Greenberg, R. Rademacher, and C. Senko, *Phys. Rev. A* **105**, 033102 (2022).
- [53] A. Osada and A. Noguchi, *J. Phys. Commun.* **6**, 015007 (2022).
- [54] G. Vrijsen, Y. Aikyo, R. F. Spivey, I. V. Inlek, and J. Kim, *Opt. Express* **27**, 33907 (2019).
- [55] S. Olmschenk and P. Becker, *Appl. Phys. B* **123**, 99 (2017).
- [56] K. Zimmermann, M. V. Okhapkin, O. A. Herrera-Sancho, and E. Peik, *Appl. Phys. B* **107**, 883 (2012).
- [57] C. Sun, K. Cui, S. Chao, Y. Wei, J. Yuan, J. Cao, H. Shu, and X. Huang, *Rev. Sci. Instrum.* **93**, 113201 (2022).
- [58] L. Schmöger, O. O. Versolato, M. Schwarz, M. Kohnen, A. Windberger, B. Piest, S. Feuchtenbeiner, J. Pedregosa-Gutierrez, T. Leopold, P. Micke, A. K. Hansen, T. M. Baumann, M. Drewsen, J. Ullrich, P. O. Schmidt, and J. R. C. López-Urrutia, *Science* **347**, 1233 (2015).
- [59] J. E. Fulford, D. Nhu-Hoa, R. J. Hughes, R. E. March, R. F. Bonner, and G. J. Wong, *J. Vac. Sci. Technol.* **17**, 829 (1980).
- [60] F. A. Londry and J. W. Hager, *J. Am. Soc. Mass Spectrom.* **14**, 1130 (2003).
- [61] J. Schmidt, D. Hönig, P. Weckesser, F. Thielemann, T. Schaez, and L. Karpa, *Appl. Phys. B* **126**, 176 (2020).
- [62] T. Leopold, S. A. King, P. Micke, A. Bautista-Salvador, J. C. Heip, C. Ospelkaus, J. R. Crespo López-Urrutia, and P. O. Schmidt, *Rev. Sci. Instrum.* **90**, 073201 (2019).
- [63] D. M. Lucas, A. Ramos, J. P. Home, M. J. McDonnell, S. Nakayama, J.-P. Stacey, S. C. Webster, D. N. Stacey, and A. M. Steane, *Phys. Rev. A* **69**, 012711 (2004).
- [64] D. James, *Appl. Phys. B* **66**, 181 (1998).
- [65] N. Otsu, *IEEE Trans. Syst., Man, Cybern.* **9**, 62 (1979).
- [66] M. R. Kamsap, C. Champenois, J. Pedregosa-Gutierrez, S. Mahler, M. Houssin, and M. Knoop, *Phys. Rev. A* **95**, 013413 (2017).
- [67] S. Bourdeauducq, whitequark, R. Jördens, D. Nadlinger, Y. Sionneau, and F. Kermarrec, *ARTIQ* (2021).
- [68] F. Splatt, M. Harlander, M. Brownnutt, F. Zähringer, R. Blatt, and W. Hänsel, *New J. Phys.* **11**, 103008 (2009).
- [69] T. Ruster, C. Warschburger, H. Kaufmann, C. T. Schmiegelow, A. Walther, M. Hettrich, A. Pfister, V. Kaushal, F. Schmidt-Kaler, and U. G. Poschinger, *Phys. Rev. A* **90**, 033410 (2014).
- [70] A. Walther, F. Ziesel, T. Ruster, S. T. Dawkins, K. Ott, M. Hettrich, K. Singer, F. Schmidt-Kaler, and U. Poschinger, *Phys. Rev. Lett.* **109**, 080501 (2012).
- [71] R. Bowler, J. Gaebler, Y. Lin, T. R. Tan, D. Hanneke, J. D. Jost, J. P. Home, D. Leibfried, and D. J. Wineland, *Phys. Rev. Lett.* **109**, 080502 (2012).
- [72] L. A. Zhukas, P. Svihra, A. Nomerotski, and B. B. Blinov, *Phys. Rev. A* **103**, 062614 (2021).
- [73] T. Manovitz, Y. Shapira, L. Gazit, N. Akerman, and R. Ozeri, *PRX Quantum* **3**, 010347 (2022).
- [74] S. Halama, T. Dubielzig, N. Orłowski, C. Torkzaban, and C. Ospelkaus, *arXiv:2204.09112*.
- [75] K. Okada, M. Wada, T. Takayanagi, S. Ohtani, and H. A. Schuessler, *Phys. Rev. A* **81**, 013420 (2010).
- [76] D. Kielpinski, C. Monroe, and D. J. Wineland, *Nature (London)* **417**, 709 (2002).
- [77] J. M. Pino, J. M. Dreiling, C. Figgatt, J. P. Gaebler, S. A. Moses, M. S. Allman, C. H. Baldwin, M. Foss-Feig, D. Hayes, K. Mayer, C. Ryan-Anderson, and B. Neyenhuis, *Nature (London)* **592**, 209 (2021).
- [78] S. van der Walt, J. L. Schönberger, J. Nunez-Iglesias, F. Boulogne, J. D. Warner, N. Yager, E. Gouillart, T. Yu, and the scikit-image contributors, *PeerJ* **2**, e453 (2014).